# Continuous spectra of the Batchelor vortex

**Xueri Mao and Spencer Sherwin**

Department of Aeronautics, Imperial College London, South Kensington, SW7 2AZ, UK

The spectra of the Batchelor vortex are obtained by discretizing its linearised evolution operator using a modified Chebyshev polynomial approximation at a Reynolds number of 1000 and zero azimuthal wave number. Three types of eigenmodes are identified from the spectra: discrete modes, potential modes and free-stream modes. The discrete modes have been extensively documented but the last two modes have received little attention. A convergence study of the spectra and pseudospectra supports the observation that discrete modes correspond to discrete spectra while the other two correspond to continuous spectra. The free-stream modes are a limiting form of the potential modes when the radial decay rate of velocity components reduces to zero. The radial form of the free-stream modes with axial and radial wave numbers is investigated and the penetration of the free-stream mode into the vortex core highlights the possibility for interaction between the potential region and the vortex core. A wave-packet pseudomode study confirms the existence of continuous spectra and predicts the locations and radial wave numbers of the eigenmodes. The pseudomodes corresponding to the potential modes are observed to be in the form of one or two wave-packets while the free-stream modes are not observed to be in the form of wave-packets.

## 1. Introduction

The Batchelor vortex is an approximate solution to the Navier-Stokes equations under a boundary-layer-type approximation obtained by Batchelor (1964) and it has been used extensively as a typical mathematical model of vortices. In this paper, the Batchelor vortex is adopted to investigate the whole spectrum of the vortex because it is widely used in the vortex stability studies and it also models trailing or jet-like vortices.

The Batchelor vortex can be represented in the cylindrical coordinates $(x, r, \theta)$ as

$$U(r) = a + e^{-r^2}, \qquad V(r) = 0, \qquad W(r) = q/r(1 - e^{-r^2}), \qquad (1.1)$$

where $q$ is the swirl strength and $q = 3$ is used throughout this paper if not otherwise stated. In the above the parameter $a$ designates the free stream velocity. It has been noted by Lessen *et al.* (1974) that the translation and inversion of the axial velocity $U(r)$ do not affect the instability of the Batchelor vortex – they only affect the frequency but the growth rates remain unchanged, so $a = 0$ is adopted in this paper. $Re$ denotes the Reynolds number, defined as $Re = \Delta U R_0/\nu$, where $\Delta U$ is the dimensional velocity excess in the core of the vortex, $R_0$ is related to the core size of the vortex and $\nu$ is the kinematic viscosity. In this paper, $Re$ is taken to be 1000 if not otherwise stated.

Most of the studies of the Batchelor vortex have focused on the evolution of perturbations inside the vortex core/shear layer, and little attention has been paid to the out-of-core region, where the flow is dominated by the algebraic decaying terms in the base flow. Taking into account the corresponding spectra, the modes of the Batchelor vortex can be classified into three broad categories:

1) Discrete modes, which correspond to a discrete spectrum. Discrete modes have

been intensively studied in both inviscid and viscous conditions since Rayleigh (1916) proposed his famous stability criterion. To date, all the reported unstable modes of the Batchelor vortex are discrete modes. There are two typical unstable discrete modes: inviscidly unstable modes (Lessen, Singh & Paillet 1974; Lessen & Paillet 1974; Heaton 2007) and viscously unstable modes (Khorrami 1991; Fabre & Jacquin 2004). Those discrete unstable modes are concentrated around the vortex core. More recently, an unstable viscous ring mode, which is spatially concentrated near a particular radius corresponding to a double critical point of the inviscid equation, has been reported by Le Dizés & Fabre (2010). The discrete mode of the Batchelor vortex decays exponentially or super-exponentially in the radial direction. The radial distribution of a typical discrete mode is shown in figure 1a.

2) Potential modes, which are part of a continuous spectrum, have an non-trivial amplitude outside of the vortex core but decay to zero at large radial values. Indeed potential modes are observed to decay much slower than the exponential/super-exponential decay rate of the discrete modes. Potential modes are asymptotically stable, but they are highly non-orthogonal and a linear combination of them could lead to strong transient growth (Obrist & Schmid 2003b; Mao 2010). The radial distribution of typical potential modes are shown in figures 1b and 1c. Potential modes have also been investigated in the potential flow region around swept bluff bodies (Obrist & Schmid 2010), where a spanwise velocity component exists due to the sweep angle and this spanwise velocity has a similar effect to the azimuthal velocity in the vortex flow. Obrist & Schmid (2003a) have demonstrated analytically that potential modes decay algebraically in the radial direction in the leading-edge boundary layer flow.

3) Free-stream modes around the Batchelor vortex, which are also part of a continuous spectrum, are similar to the well-documented "continuous spectrum" in the boundary layer flow. Free-stream mode is a limiting form of the potential modes as the radially decay rate tends to zero. These are the only modes surviving in the far free stream. Most of the published work on free-stream modes/spectra is related to the continuous spectrum of the one-variable Orr-Somerfeld equation in boundary layer flow. The existence of free-stream boundary layer modes of the Orr-Somerfeld equation for a Blasius boundary layer was conjectured by Jordinson (1970) and affirmed both by a numerical approach (Mack 1976) and an analytical expression (Gustavsson 1979; Grosch & Salwen 1978). It was found that the free-stream modes are small in the boundary layer and oscillatory in the free stream. Zaki & Saha (2009) have demonstrated that the free-stream modes with small axial wave numbers penetrate the boundary layer and therefore provide a mechanism to introduce free stream turbulence into the boundary layer. The free-stream spectrum however has not been very actively investigated in the vortex flows which are dependent on three velocity components and where the governing equations cannot be reduced to a one-variable equation. Fabre et al. (2006) noted that there would be a free-stream spectrum in the vortex flow, although they did not provide a mathematical investigation of this observation. The radial distribution of a typical free-stream mode is shown in figure 1d.

The remainder of this paper is organised as follows: in §2, we introduce the governing equations; in §3, we describe the modified Chebyshev discretization used to discretize the governing equations; in §4 we validate the discretization by comparing the results against published values; in §5, we present the map of spectra and pseudospectra of the Batchelor vortex and identify the three typical modes; in §6, we apply the wave-packet pseudomode method to further investigate the spectrum of the vortex corresponding to eigenmodes with wave packet forms; finally in §7 we summarise the results. The existence and continuity of the free-stream spectrum are verified in appendix B.
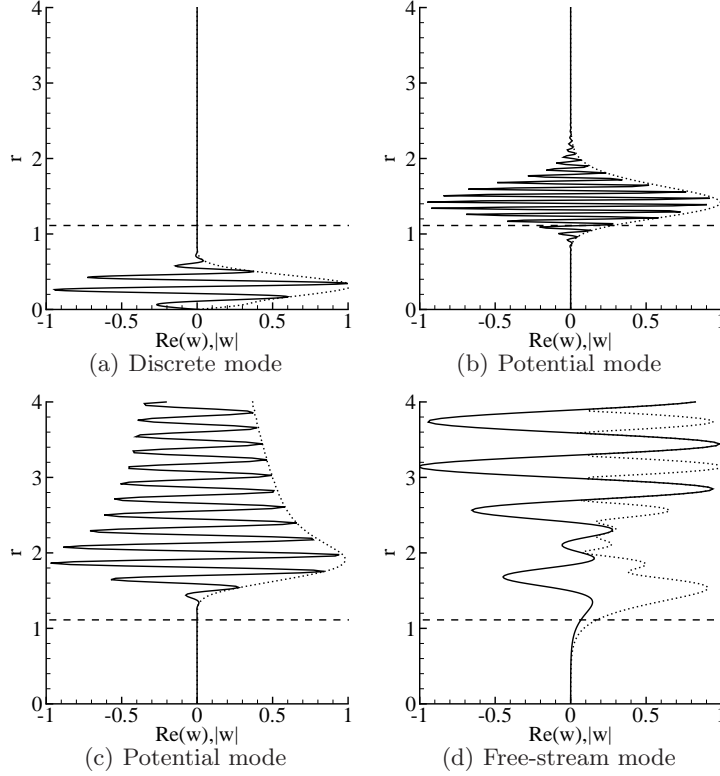
FIGURE 1. Swirl velocity components for typical (a) discrete mode, (b,c) potential modes and (d) free-stream mode at azimuthal wave number $m = 0$, axial wave number $k = 10$, swirl strength $q = 3$ and Reynolds number $Re = 1000$. All these parameters will be used in the following investigations is not otherwise stated. The real part $\mathrm{Re}(w)$ is denoted by solid lines while the absolute value $|w|$ is illustrated by dotted lines. The dashed line $r = 1.122$ denotes the position of core radius of the Batchelor vortex, corresponding to the maximum azimuthal velocity $W = 0.639q$ (see equation (1.1)).

## 2. Governing equations

Assuming the fluid to be Newtonian and the flow incompressible, the relevant equations of motion for the primitive variables (velocities, pressure) are the incompressible Navier-Stokes equations:

$$\partial_t \hat{\boldsymbol{u}} = -(\hat{\boldsymbol{u}} \cdot \nabla)\hat{\boldsymbol{u}} - \nabla\hat{p} + Re^{-1}\nabla^2\hat{\boldsymbol{u}}, \qquad \text{with} \qquad \nabla \cdot \hat{\boldsymbol{u}} = 0,$$

where $\hat{\boldsymbol{u}}(x, r, \theta; t)$ is the velocity field and $\hat{p}(x, r, \theta; t)$ is the modified pressure incorporating the constant density.

Decomposing the flow field as a summation of a base flow field, whose velocity vector and modified pressure are denoted by $(\boldsymbol{U}, P)$, and a perturbation field, whose velocity vector and modified pressure are denoted by $(\boldsymbol{u}', p')$, by substituting $\hat{\boldsymbol{u}} = \boldsymbol{U} + \boldsymbol{u}'$ and $\hat{p} = P + p'$ into the incompressible Navier-Stokes equations and then linearising the advection term, we obtain

$$\partial_t \boldsymbol{u}' = -(\boldsymbol{U} \cdot \nabla)\boldsymbol{u}' - (\boldsymbol{u}' \cdot \nabla)\boldsymbol{U} - \nabla p' + Re^{-1}\nabla^2\boldsymbol{u}', \qquad \text{with} \qquad \nabla \cdot \boldsymbol{u}' = 0, \quad (2.1)$$

where the base flow velocity vector $\boldsymbol{U} = (U, V, W)$ is defined in equations (1.1).

Decompose the perturbations in the axial and azimuthal directions and consider the

perturbations in the local form:

$$(\boldsymbol{u}', p') = (u', v', w', p') = [u(r), v(r), w(r), p(r)]\exp(\mathrm{i}kx + \mathrm{i}m\theta + \sigma t), \qquad (2.2)$$

where $k$ is the axial wave number, $m$ is the azimuthal wave number and $\sigma$ is the growth rate.

Substituting equation (2.2) into (2.1) and eliminating $u$ and $p$ through standard algebraic and differential manipulations, the governing equations can be expressed as

$$\sigma \begin{bmatrix} \boldsymbol{L}_{vv} & \boldsymbol{L}_{vw} \\ \boldsymbol{L}_{wv} & \boldsymbol{L}_{ww} \end{bmatrix} \begin{bmatrix} v \\ w \end{bmatrix} = \begin{bmatrix} \boldsymbol{R}_{vv} & \boldsymbol{R}_{vw} \\ \boldsymbol{R}_{wv} & \boldsymbol{R}_{ww} \end{bmatrix} \begin{bmatrix} v \\ w \end{bmatrix},$$

$$\text{or} \qquad \sigma \begin{bmatrix} v \\ w \end{bmatrix} = \begin{bmatrix} \boldsymbol{L}_{vv} & \boldsymbol{L}_{vw} \\ \boldsymbol{L}_{wv} & \boldsymbol{L}_{ww} \end{bmatrix}^{-1} \begin{bmatrix} \boldsymbol{R}_{vv} & \boldsymbol{R}_{vw} \\ \boldsymbol{R}_{wv} & \boldsymbol{R}_{ww} \end{bmatrix} \begin{bmatrix} v \\ w \end{bmatrix} = \boldsymbol{D} \begin{bmatrix} v \\ w \end{bmatrix}. \qquad (2.3)$$

The details of the entries of the matrices are given in appendix A.

We see from equation (2.3) that the growth rate $\sigma$ is an eigenvalue of the matrix $\boldsymbol{D}$. In the free stream where only the free-stream modes survive, $\boldsymbol{L}_{vw} = \boldsymbol{L}_{wv} = \boldsymbol{R}_{vw} = \boldsymbol{R}_{wv} = 0$, and so $v$ and $w$ are decoupled. For axisymmetric modes ($m = 0$), in the potential region, where the exponential terms of the base flow have decayed to zero and the continuous spectrum dominates, $\boldsymbol{L}_{vw} = \boldsymbol{L}_{wv} = \boldsymbol{R}_{wv} = 0$, and $v$ and $w$ are partially decoupled.

The boundary conditions of $(v, w)$ depend on the value of $m$. At $m = 0$ the boundary conditions of $(u, v, w)$ can be expressed as (Lessen, Singh & Paillet 1974)

$$\begin{aligned} r = 0 &: \mathrm{d}u/\mathrm{d}r = v = w = \mathrm{d}p/\mathrm{d}r = 0, \\ r \to \infty &: u = v = w = p = 0. \end{aligned} \qquad (2.4)$$

Differentiate the mass continuous or divergence free equation in the linearised governing equations twice to transfer the boundary conditions of $(u, v, w)$ to the boundary conditions of $(v, w)$ for equation (2.3):

$$\begin{aligned} r = 0 &: v = 0, \mathrm{d}^2v/\mathrm{d}r^2 = 0, w = 0, \\ r \to \infty &: v = 0, w = 0, \mathrm{d}v/\mathrm{d}r = 0. \end{aligned} \qquad (2.5)$$

## 3. Discretization

A modified Chebyshev polynomial method is used to discretize the governing equations. The Chebyshev method has been previously applied to the stability analysis of vortex flow by Khorrami (1991), who used a staggered grid approach for the pressure and momentum components of the problem. In this discretization, the velocities are evaluated at the collocation points $y_i$, which are the extrema of the last retained Chebyshev polynomial ($\Gamma_M(y)$) in the truncated series, while the pressure and the continuity equations are evaluated at the collocation points $y_{i+1/2}$, which are the roots of $\Gamma_M(y)$. Since then the Chebyshev polynomial method has been used in a number of the stability studies of vortex flow (Khorrami 1991, 1992; Fabre & Jacquin 2004; Heaton 2007; Abid 2008).

There are two strategies for imposing boundary conditions in the Chebyshev discretization, boundary bordering and basis modification, as described by Boyd (2001). The boundary bordering method can lead to spurious eigenvalues induced by the extra algebraic constraints to the system (Schmid & Henningson 2001). Basis modification involves the replacement of the original basis functions with modified functions that each satisfies the homogeneous boundary conditions. This basis modification method has been applied by Weideman & Reddy (2000), McKernan (2006), Boyd (2001), Joshi (1996), Heinrichs (1989), and Heinrichs (1991) and is adopted in the current study.

As is standard practise, the range of radial coordinate $r$ is truncated from $[0, +\infty)$ to $[0, R]$. The problem is then mapped from physical space $\{r | r \in [0, R]\}$ to Chebyshev interval $\{y | y \in [-1, 1]\}$ via a linear mapping function $y = 2r/R - 1$. We note that the collocation points are not concentrated in the vortex core since we are interested in both the core region and potential/free-stream regions. A non-linear mapping function $r = \exp^{y \lg R}$ was also considered to stretch the grid for large $R$, but it was observed that the conditioning number of the matrix is significantly increased for larger values of $R$. Therefore we apply a linear fixed range and check the independence of the results with respect to $R$.

The Chebyshev polynomial functions can be written as

$$\Gamma_1(y) = 1, \qquad \Gamma_2(y) = y, \qquad \Gamma_{i>2}(y) = 2y\Gamma_{i-1} - \Gamma_{i-2}.$$

This expansion is modified to satisfy the boundary conditions expressed in equations (2.5). Here only the modification corresponding to $m = 0$ is presented while the modification at other azimuthal wave numbers can be obtained analogously.

The modified polynomial basis for $v$ is defined as

$$\Xi_1 = \Gamma_1, \; \Xi_2 = \Gamma_2, \; \Xi_3 = \Gamma_3 - \Gamma_1,$$
$$\Xi_4 = (\Gamma_4 - \Gamma_2) - 2(\Gamma_3 - \Gamma_1),$$
$$\Xi_{i>4,\text{odd}} = \Gamma_i - \Gamma_1 - \frac{1}{4}(i-1)^2(\Gamma_3 - \Gamma_1)$$
$$+ \frac{1}{96}[(i-1)^4 - 4(i-1)^2](\Gamma_4 - 2\Gamma_3 - \Gamma_2 + 2\Gamma_1),$$
$$\Xi_{i>4,\text{even}} = \Gamma_i - \Gamma_2 - \frac{1}{4}(i^2 - 2i)(\Gamma_3 - \Gamma_1)$$
$$+ \frac{1}{96}[-(i-1)^4 - 2(i-1)^2 + 3](\Gamma_4 - 2\Gamma_3 - \Gamma_2 + 2\Gamma_1).$$

This basis satisfies $\Xi_{i>2}(\pm 1) = 0$, $\frac{d\Xi_{i>4}}{dy}(1) = 0$ and $\frac{d^2\Xi_{i>4}}{dy^2}(-1) = 0$, so that $\Xi_{i>4}$ satisfies the boundary conditions of $v$.

The modified polynomial basis for $w$ is defined as

$$\Theta_1 = \Gamma_1,$$
$$\Theta_2 = \Gamma_2,$$
$$\Theta_{i>2,\text{odd}} = \Gamma_i - \Gamma_1,$$
$$\Theta_{i>2,\text{even}} = \Gamma_i - \Gamma_2.$$

This basis satisfies $\Theta_{i>2}(\pm 1) = 0$.

In the Chebyshev space, the Gauss-Lobatto points are used

$$y_i = \cos\left((i-1)\pi/(M-1)\right), \qquad i = 1, 2, 3, ..., M,$$

where $M$ is the span of the Chebyshev basis and $y_i$ correspond to the extrema of the last retained Chebyshev polynomial before modification. The two outer boundary conforming modified expansion modes are reordered to the second and the fourth places in the matrix. Therefore the first four rows of the discretized equations represent the implementation of boundary conditions and these four equations are decoupled from the rest of system.

Finally the partitioned Chebyshev expansions for $v$ can be represented as

$$\begin{bmatrix} v(y_3) \\ \vdots \\ v(y_{M-2}) \end{bmatrix} = \begin{bmatrix} \Xi_5(y_3) & \cdots & \Xi_M(y_3) \\ \vdots & \ddots & \vdots \\ \Xi_5(y_{M-2}) & \cdots & \Xi_M(y_{M-2}) \end{bmatrix} \begin{bmatrix} \tilde{v}_5 \\ \vdots \\ \tilde{v}_M \end{bmatrix},$$

or more compactly as

$$v = \boldsymbol{\Xi}\tilde{v}, \tag{3.1}$$

and the partitioned expansion for $w$ is

$$
\begin{bmatrix} w(y_3) \\ \vdots \\ w(y_{M-2}) \end{bmatrix} =
\begin{bmatrix} \Theta_3(y_3) & \cdots & \Theta_{M-2}(y_3) \\ \vdots & \ddots & \vdots \\ \Theta_3(y_{M-2}) & \cdots & \Theta_{M-2}(y_{M-2}) \end{bmatrix}
\begin{bmatrix} \tilde{w}_3 \\ \vdots \\ \tilde{w}(y_{M-2}) \end{bmatrix},
$$

or more compactly as

$$w = \boldsymbol{\Theta}\tilde{w}, \tag{3.2}$$

where $\tilde{v}_i$ and $\tilde{w}_i$ are unknown coefficients. Note that in the expansion of $w$, $w(y_2)$ and $w(y_{M-1})$ are not expanded and the two polynomials $\Theta_{M-1}$ and $\Theta_M$ are discarded to obtain a square expansion matrix.

It can be demonstrated from the properties of the modified basis that $\tilde{v}_1 \sim \tilde{v}_4 = 0$ and $\tilde{w}_1 \sim \tilde{w}_2 = 0$, so the first four equations in the expansion of $v$ and the first two equations in the expansion of $w$, which represent the enforcement of boundary conditions, are separated from the remaining parts of the expansion forms.

Substituting the expansions (3.1) and (3.2) into equation (2.3) results in

$$
\sigma \begin{bmatrix} \tilde{v} \\ \tilde{w} \end{bmatrix} = \tilde{\boldsymbol{D}} \begin{bmatrix} \tilde{v} \\ \tilde{w} \end{bmatrix}.
$$

The matrix of operator $\boldsymbol{D}$ can be obtained from:

$$
\boldsymbol{D} = \begin{bmatrix} \boldsymbol{\Xi} & 0 \\ 0 & \boldsymbol{\Theta} \end{bmatrix} \tilde{\boldsymbol{D}} \begin{bmatrix} \boldsymbol{\Xi}^{-1} & 0 \\ 0 & \boldsymbol{\Theta}^{-1} \end{bmatrix}. \tag{3.3}
$$

At other non-zero azimuthal wave numbers, the Chebyshev polynomial basis can be modified similarly to satisfy the boundary conditions for velocity components and obtain the discretized matrix $\boldsymbol{D}$.

## 4. Validation

After applying the modified Chebyshev polynomial method to discretize the matrix $\boldsymbol{D}$, the eigenvalues of the discretized matrix are calculated using the QR algorithm. The leading eigenvalues $\sigma$ of matrix $\boldsymbol{D}$ obtained using the present method are compared against published data (Fabre & Jacquin 2004) and theoretical results, as shown in table 1. The leading eigenvalues from different methods agree up to four significant figures. The most unstable mode converges rapidly with respect to $M$ owing to the large growth rate. The convergence of the leading potential mode requires a far larger number of Chebyshev modes than the most unstable mode and the growth rate of the leading potential mode depends on the value of $R$. This dependence occurs because although the potential modes decay in the far field, a larger radial domain is required for it to be sufficiently independent of the far-field boundary conditions.

## 5. Spectra and pseudospectra

As suggested in section §1, the spectrum of operator $\boldsymbol{D}$ can be divided into three parts: a discrete spectrum, a potential spectrum and a free-stream spectrum. It will be shown

| | $M$ | $R$ | $\sigma$ | | $M$ | $R$ | $\sigma$ |
|---|---|---|---|---|---|---|---|
| current method | 20 | 10 | 0.3138 | current method | 100 | 10 | -0.1003 |
| | 30 | 10 | 0.3240 | | 200 | 10 | -0.1003 |
| | 40 | 10 | 0.3245 | | 300 | 10 | -0.1003 |
| | 50 | 10 | 0.3245 | | 300 | 12 | -0.1002 |
| | 20 | 20 | 0.2769 | | 300 | 14 | -0.1001 |
| | 30 | 20 | 0.3276 | | 300 | 16 | -0.1001 |
| | 40 | 20 | 0.3254 | | 300 | 18 | -0.1001 |
| | 50 | 20 | 0.3245 | | 300 | 20 | -0.1 |
| Fabre & Jacquin (2004) | | | 0.3245 | Theoretical value | | | -0.1 |

TABLE 1. Validation against published results and theoretical values. $M$ is the number of Chebyshev polynomials, $R$ is the radial length of the domain and $\sigma$ is the growth rate. Left: Leading unstable discrete eigenvalue at azimuthal wave number $m = -3$, swirl strength $q = 0.761$, axial wave number $k = 1.659$ and Reynolds number $Re = 1000$. Right: Leading eigenvalue in the continuous spectrum at $m = 0$, $q = 3$, $k = 10$ and $Re = 1000$. The theoretical value of the leading continuous eigenvalue $-k^2/Re = -0.1$ is obtained in appendix B.

later that the last two spectra are continuous. In the following study, $m = 0$ and $k = 10$ are used if not otherwise stated. The three typical spectra can be also obtained at other wave numbers.

From the leading discrete spectrum of $\boldsymbol{D}$ shown in figure 2a, we see that as $M$ and $R$ increase, the eigenvalues in the discrete spectrum converge to fixed points in the complex plane. The relative difference of these discrete eigenvalues is within 0.1% when $M$ is increased from 600 to 800 and $R$ is varied from 14 to 40. Discrete eigenvalues may pass the imaginary line to reach the unstable region at some combinations of parameters and we note that all the unstable modes are discrete modes. The leading unstable eigenvalue in the discrete spectrum has been used to validate the code in table 1. Inspecting the radial distribution of discrete modes (see figure 1), we see that the discrete modes decay exponentially or super-exponentially in the radial direction towards far field. A similar exponential/super-exponential decay of discrete modes has also been reported by Obrist & Schmid (2003a) in the leading-edge boundary layer flow.

Instead of converging to discrete points, the leading eigenvalues in the continuous spectrum approach the real axis to form a continuous line, which is part of the free-stream spectrum (see figure 2b). These free-stream eigenvalues have converged to three significant figures with respect to $M$ at $R = 14$. Using larger values of $M$ only affect the high frequency spectrum, which is far from the imaginary axis and is not shown in this subfigure. At fixed values of $M$, the eigenvalues converge to the real axis for increasing $R$, as predicted theoretically in appendix B. As previously mentioned, this $R$ dependency occurs because the free-stream eigenvectors oscillate in the free stream and the radial extension of the computational domain diminishes the termination effects of the far-flow-field boundary conditions. The convergence of the leading free-stream eigenvalue has been used to validate the code in table 1, where we see that the leading continuous eigenvalue converges much more slowly than the leading discrete eigenvalue.

From the full spectrum of our discretisation shown in figure 2e, we note that besides the discrete spectrum and the continuous line, other eigenvalues (apparently randomly) fill an approximately rectangular region to form another continuous spectrum, which we refer to as the potential spectrum.

The values of $M$ and $R$ we have considered do not affect the shape of the spectra significantly, although at larger $M$, more high frequency eigenvalues are resolved. Taking

into consideration both the simulation speed and accuracy, $R = 14$ and $M = 800$ are applied in the following investigation.

The pseudospectrum is considered as a complementary analysis technique to analyze the operator $\boldsymbol{D}$ and is calculated via a singular value decomposition. Considering a point $\omega = \mathrm{Re}(\omega) + \mathrm{iIm}(\omega)$ in the complex plane, from the singular value decomposition of the matrix $(\omega\boldsymbol{I} - \boldsymbol{D})$, one observes that

$$(\omega\boldsymbol{I} - \boldsymbol{D})u_s = \epsilon v_s, \tag{5.1}$$

where $\boldsymbol{I}$ is the unit matrix and $u_s$ and $v_s$ are the right and left singular vectors corresponding to the minimum singular value $\epsilon$. Since the singular vectors are orthonormal, we have

$$||(\boldsymbol{D} - \omega\boldsymbol{I})u_s|| = ||\epsilon v_s|| = \epsilon. \tag{5.2}$$

$||\cdot||$ represents the L-2 norm of vectors (Trefethen 2005). Clearly the value of $\epsilon$ indicates the accuracy of the pair $(\omega, u_s)$ as an eigenvalue/vector pair of the matrix $\boldsymbol{D}$. If $(\omega, u_s)$ is an exact pair of eigenvalue/vector of $\boldsymbol{D}$, then $\epsilon = 0$.

Figure 2c illustrates the pseudospectra surrounding the leading discrete spectrum. The pseudospectra converge to a consistent boundary with respect to $M$ and $R$. The pseudospectra are in the form of circles surrounding the eigenvalues especially when the discrete spectra are independent from the free-stream continuous spectrum with $\mathrm{Im}(\sigma) = 0$. The circular form of these pseudospectra further confirms that the corresponding spectrum is discrete.

From figure 2d, we see that the pseudospectra around the potential spectrum converge to a fixed bounding region with respect to both $M$ and $R$. For the range of $\epsilon$ considered, these pseudospectra are quite different to the pseudospectra around discrete spectra. However instead of appearing in the form of circles surrounding the eigenvalues, the pseudospectra appears as lines bounding the spectrum which gets closer to the spectrum as $\epsilon$ decreases. The form of these pseudospectra suggests that the potential spectrum could be continuous, although this can not be conclusively stated from this type of analysis.

The pseudospectrum illustrated in figure 2e corresponds to $\epsilon = 10^{-5}$. This pseudospectrum indicates that any point enclosed by this pseudospectrum are sufficiently close to be eigenvalues to within a tolerance of $10^{-5}$.

A typical eigenvector corresponding to the discrete spectrum (point "a" in figure 2e) is shown in figure 1a. We see that the energy is concentrated in the vortex core, which is typical for all the reported asymptotically unstable modes. At appropriate combinations of parameters, the discrete spectrum crosses the imaginary axis and the vortex flow becomes asymptotically unstable. Most of the documented modes of the Batchelor vortex, such as the helical unstable modes (Lessen, Singh & Paillet 1974; Lessen & Paillet 1974; Heaton 2007) and viscously unstable modes (Khorrami 1991; Fabre & Jacquin 2004) are discrete modes.

Typical potential modes corresponding to the continuous spectrum (points "b" and "c" in figure 2e) are shown in figure 1b and 1c. The continuous spectrum is restricted in an approximated rectangular region. For increasing $M$, more high frequency modes (distant from the imaginary axis) are resolved, so the continuous spectrum is semi-infinite. The pseudospectrum around the continuous spectrum indicates that all the points in the region are estimates of the eigenvalues of $\boldsymbol{D}$ to within $10^{-5}$ (see figure 2e). The potential mode decays in the radial direction and as the potential eigenvalue approaches the real axis, the corresponding potential mode decays more slowly in the radial direction. Finally
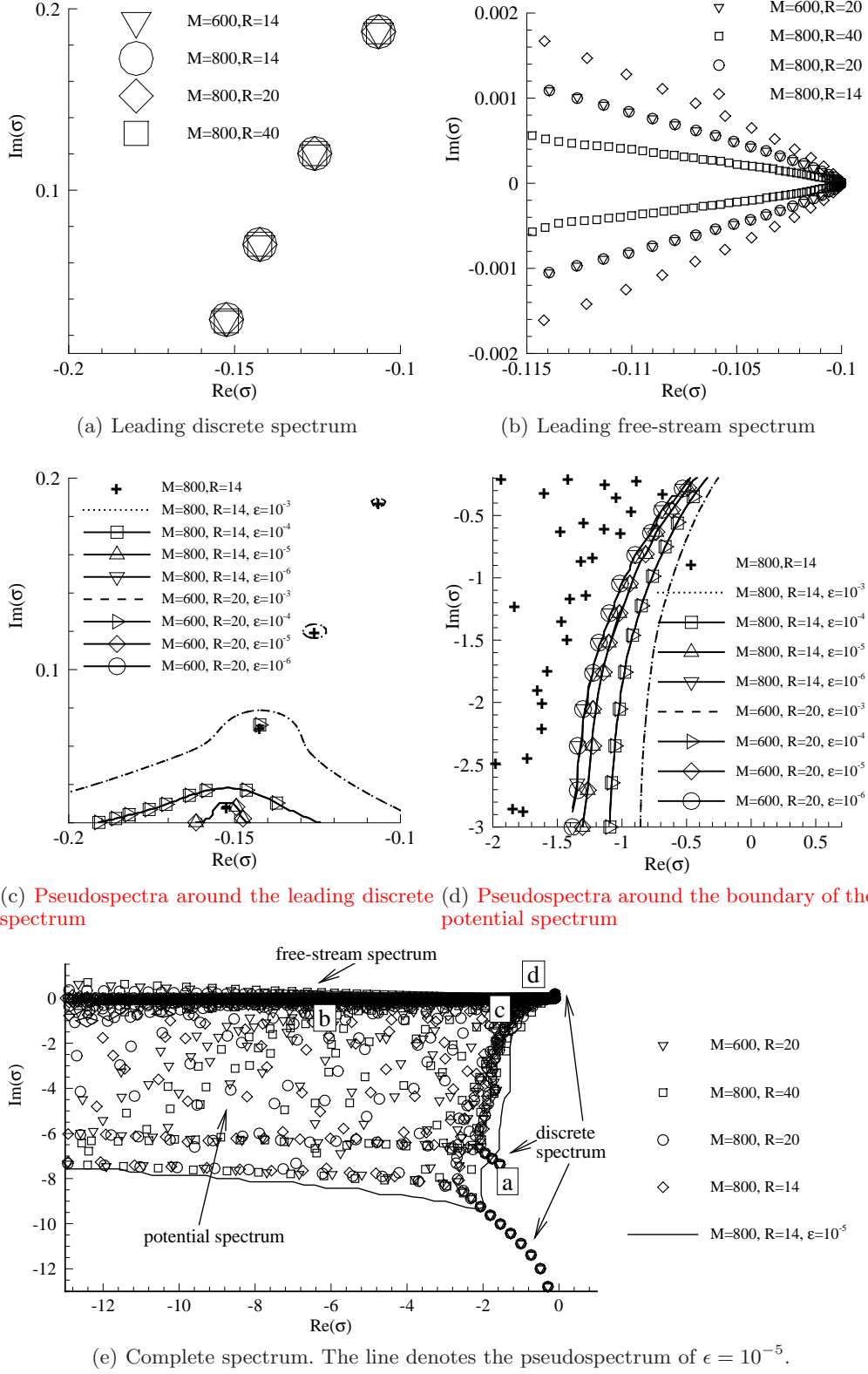
(a) Leading discrete spectrum

(b) Leading free-stream spectrum

(c) Pseudospectra around the leading discrete spectrum

(d) Pseudospectra around the boundary of the potential spectrum

(e) Complete spectrum. The line denotes the pseudospectrum of $\epsilon = 10^{-5}$.

FIGURE 2. Convergence of the spectra and pseudospectra of $\boldsymbol{D}$. The spectrum is denoted by points while the pseudospectra is represented by lines. The azimuthal and axial wave numbers, Reynolds number and swirl strength are the same as used in figure 1.
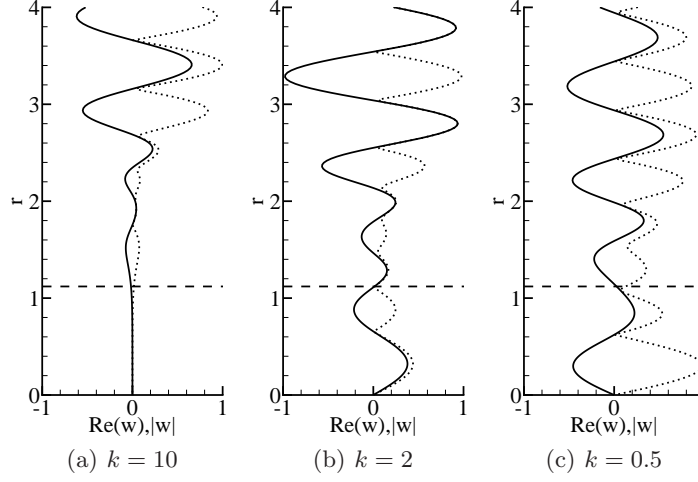
FIGURE 3. Scaled radial distribution of free-stream modes at various axial wave numbers. The solid lines denotes the real part while the absolute value is represented by the dotted lines. The radial wave number is fixed at $n = 2\pi$, where $n$ is the radial wave number (see appendix B). The dashed lines $r = 1.122$, where the azimuthal velocity reaches maxima, represent the core radius of the Batchelor vortex.

when the eigenvalue reaches the real axis, the corresponding eigenvector becomes a free-stream mode, which oscillates in the far field without decay.

A typical free-stream mode corresponding to point "d" in figure 2e is shown in figure 1d. The existence of the free-stream spectrum, which is located on the real axis from $-\infty$ to $-k^2/Re$, is verified in appendix B. Under inviscid or axially homogeneous conditions, the leading free-stream mode becomes neutrally stable.

Similar to the "continuous mode" of the Orr-Somerfeld equation, free-stream modes with smaller axial wave numbers (larger wave length) penetrate into the vortex core while axially short waves are sheltered from the vortex core, as shown in figure 3. These modes, especially the one at $k = 0.5$ exhibit a slight decay in the radial direction owing to the limited radial region shown in these figures. If these figures are extended from $r = 0 - 4$ to $r = 0 - 8$, they no longer appear to decay. This decay suggests that free-stream modes peak at finite values of $r$, and this problem is addressed in detail in section 6. In terms of the radial wavenumber the result is reversed. Free-stream modes with larger radial wave numbers, denoted by $n$ (see appendix B), penetrate into the vortex core when the axial wave number is fixed.

## 6. Wave-packet pseudomodes

Owing to the sensitivity of the spectrum to the discretization, the classic eigenvalue solver is not a useful tool to study the continuous spectrum. In this section, we turn to a pseudospectrum/mode approach to further investigate the nature of the continuous spectrum.

### 6.1. *Twist conditions for wave-packet pseudomodes*

The linear evolution operator of the Batchelor vortex has exponentially large resolvent norms, defined as $||(\omega \boldsymbol{I} - \boldsymbol{D})^{-1}||$, even when $\omega$ is far from the eigenspectrum in the complex plane. These large norms can be explained by the existence of pseudofunctions

in the form of localised wave packets, which, although they may not satisfy the differential equations or the boundary conditions exactly, satisfy them with exponentially small error.

We can see from the governing equations (2.1) that the highest derivatives are multiplied by a small factor $h = Re^{-1/2}$, provided that the Reynolds number is large enough. The classical method of deriving results for wave-packet pseudomodes of this kind of operator is the Wentzel-Kramers-Brillouin-Jeffreys (WKBJ) approximation, in which a wave packet is constructed that is localised with respect to both the space variable and the wave number. This approach requires the coefficients of the operator to be smooth. Trefethen (2005) proposed an alternative approach that requires the *winding number* of the symbol curve (as defined below) with respect to a point increases by one as the spatial coordinate increases to pass this point. However, it is found that the difference between these approaches is substantial rather than only transforming the condition from one approach to another. For at least some problems with smooth coefficients that violate the winding number condition, the pseudospectral effects are structurally unstable (sensitive to discretization or boundary perturbations) and vanish when the coefficients are perturbed in a non-smooth manner. By contrast, the effects associated with operators that satisfy the winding number condition are robust (Trefethen 2005).

The symbol or the Fourier transformed operator of the linear evolution operator can be obtained by substituting $(v, w) = (\tilde{v}, \tilde{w})e^{i\beta r/h}$ into equations (2.3) and transferring the differential operator to a polynomial operator:

$$\boldsymbol{f}(\beta, r) = \sigma = \frac{\mathcal{M} + \mathcal{F}\mathcal{H} \pm \sqrt{\mathcal{M}^2 + \mathcal{F}^2\mathcal{H}^2 - 2\mathcal{M}\mathcal{H}\mathcal{F} + 4\mathcal{E}\mathcal{G}\mathcal{F}}}{2\mathcal{F}}, \tag{6.1}$$

where $\boldsymbol{f}$ denotes the symbol and the expressions of $\mathcal{E}, \mathcal{F}, \mathcal{G}, \mathcal{H}, \mathcal{M}$ are given in appendix C. The same result can be obtained by adopting the matrix form of the symbol as used by Obrist & Schmid (2008) for a differential operator with two dependent variables. From equation (6.1), we see that owing to the square root operator the symbol has two solutions. The solution corresponds to $\text{Im}(\pm\sqrt{\mathcal{M}^2 + \mathcal{F}^2\mathcal{H}^2 - 2\mathcal{M}\mathcal{H}\mathcal{F} + 4\mathcal{E}\mathcal{G}\mathcal{F}}) \geqslant 0$ is denoted as solution (i), while the other is denoted as solution (ii).

The twist condition (winding number condition) for the existence of wave-packet pseudomodes can be expressed as

$$\text{Im}\left\{\frac{\partial \boldsymbol{f}}{\partial r} \Big/ \frac{\partial \boldsymbol{f}}{\partial \beta}\right\} < 0, \tag{6.2}$$

or

$$\text{Im}\Big\{\frac{\partial_r \mathcal{F}\boldsymbol{f}^2 - (\partial_r\mathcal{M} + \mathcal{H}\partial_r\mathcal{F} + \mathcal{F}\partial_r\mathcal{H})\boldsymbol{f} + \mathcal{H}\partial_r\mathcal{M} + \mathcal{M}\partial_r\mathcal{H} - \mathcal{G}\partial_r\mathcal{E} - \mathcal{E}\partial_r\mathcal{G}}{\partial_\beta \mathcal{F}\boldsymbol{f}^2 - (\partial_\beta\mathcal{M} + \mathcal{H}\partial_\beta\mathcal{F} + \mathcal{F}\partial_\beta\mathcal{H})\boldsymbol{f} + \mathcal{H}\partial_\beta\mathcal{M} + \mathcal{M}\partial_\beta\mathcal{H}}\Big\} < 0. \tag{6.3}$$

At a point $(\beta_*, r_*)$ where the twist condition is satisfied, there exists a pseudomode with exponentially small error, denoted as $w_*$, in the form of wave packet corresponding to the symbols given by $\boldsymbol{f}_* = \boldsymbol{f}(\beta_*, r_*)$. This pseudomode is located at $r = r_*$ with radial wave number $\beta = \beta_*$, and it approaches the exact eigenvalue as $h$ decreases:

$$\frac{||(\boldsymbol{D} - \boldsymbol{f}_* I)w_*||}{||w_*||} \leqslant K^{-1/h}, \tag{6.4}$$

$$\frac{|w_*(r)|}{\max_r |w_*(r)|} \leqslant C_1 \exp(-C_2(r - r_*)^2/h), \tag{6.5}$$

where $K > 1$ and $C_1, C_2 > 0$.

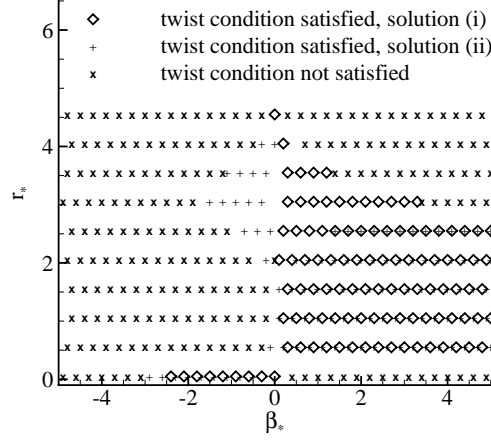The symbol is closely related to the eikonal equation in the WKBJ approximation,

FIGURE 4. Ranges of $\{\beta_*, r_*\}$ for which the twist condition is satisfied (-) or not ($\times$).

where the pseudomode at $r = r_*$ is approximated by the leading term, such as

$$w_* = \exp(\mathrm{i}\beta_* r/h + C_3(r - r_*)^2), \tag{6.6}$$

and then the real part of $C_3$ is required to be negative so that the pseudomode peaks at $r = r_*$ (Bender & Orszag 1978; Obrist & Schmid 2009). Here $C_3 < 0$ has a similar effect as $C_2 > 0$ in the twist condition.

Clearly the twist condition is only satisfied when $\boldsymbol{f}$ is dependent on $r$. In the far field when $r \to \infty$ and $\boldsymbol{f}$ becomes independent of $r$, $C_2 > 0$ is violated, and so the twist condition is not satisfied in this region. Therefore, there are no wave-packet pseudomodes in the far field. This is also confirmed by the oscillating absolute value of free-stream modes discussed above, which is not in the form of a wave packet.

### 6.2. *Wave packet pseudomodes of the Batchelor vortex*

Figure 4 illustrates the range of $(\beta_*, r_*)$ where the twist condition is satisfied or not. We see that the twist condition is not satisfied almost everywhere at $\beta_* < 0$. Since the pseudomode with radial wave number $\beta_* = 0$ is physically meaningless, in the following study we only investigate the positive values of $\beta_*$. For $r_* > 5$ or $r_* = 0$, the twist condition is also not satisfied, indicating that all the pseudomodes peak at $r_* < 5$ and that the axial boundary modes do not exist in the form of wave packets owing to the zero Dirichlet axial boundary conditions.

As stated above, the prediction of wave-packet pseudomode method is expected to be better at smaller $h$ or equivalently larger Reynolds number. Figure 5 shows the symbol curves at three Reynolds numbers $Re = 10^3, 10^4$ and $10^5$. The points where the twist condition is not satisfied is marked by "$\times$". Since the twist condition is not satisfied almost everywhere for $\beta < 0$ (see figure 4) , the negative $\beta_*$ branches of symbol curves are not illustrated for clarity. As expected, at increasing Reynolds number when the prediction of the wave-packet pseudomode method becomes more reliable, the twist condition is not satisfied only at the top and bottom boundary of the rectangular region. The upper boundary of the pseudomode region corresponds to $r_* \to \infty$ and $\boldsymbol{f}_* \to -\beta_*^2 - k^2/Re$, so the upper boundary of the pseudomode region starts at $-k^2/Re$ and extends to $-\infty$ as $\beta_*$ increases, overlapping with the free-stream spectrum. The upper boundary of the rectangular region where the twist condition is not satisfied therefore indicates that there are no wave-packet pseudomodes along the negative real axis from $-\infty$ to $-k^2/Re$, which
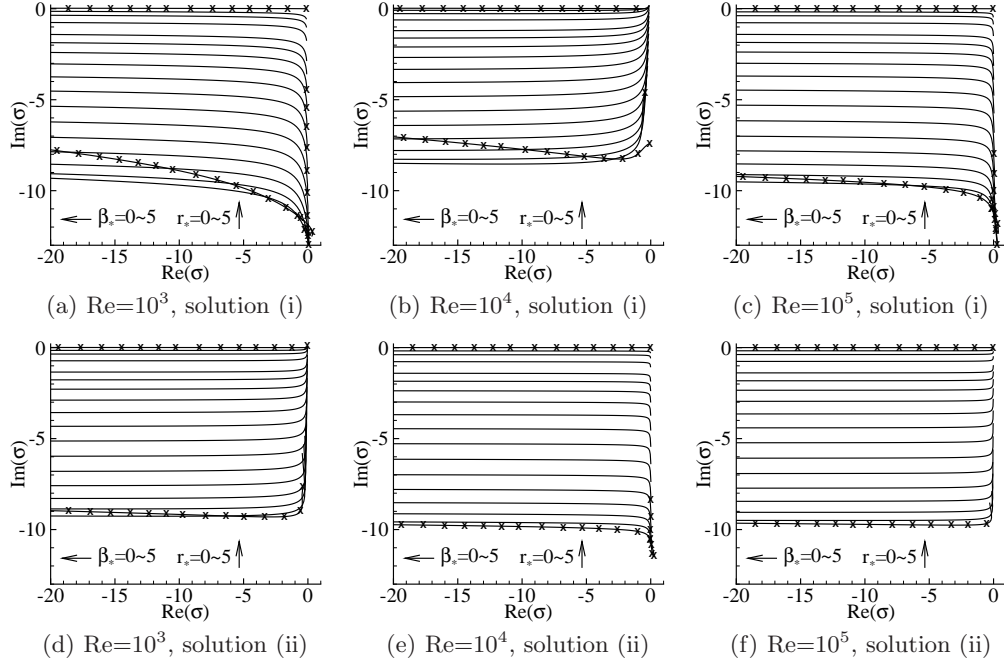
FIGURE 5. Symbol curves with $\beta_* > 0$. "$\times$" marks the points where the twist condition is not satisfied. The arrows indicate the direction in which $\beta_*$ or $r_*$ increases.

is consistent with the result in section 5 that the free-stream modes are not in the form of wave packets.

Setting $y = 0$, we get the bottom boundary of the rectangular region from equation (6.1), that is $\text{Im}(\sigma) = -ik$. The bottom boundary corresponds to axial boundary modes, which have been excluded by imposing zero Dirichlet axial boundary conditions.

As $\beta_* \to 0$, the right boundary of the pseudomode region is obtained from the two solutions of equation (6.1), that is $\boldsymbol{f}_* = (-\frac{1}{r_*^2} - k^2)/Re - ikU$ or $\text{Re}(\boldsymbol{f}_*) = \frac{(3/r_*^2+k^2)(1/r_*^2-k^2)}{(1/r_*^2+k^2)Re}$. Clearly the second solution can reach the right-half plane. As $r_*$ decreases, a smaller value of $k$ results in the penetration of pseudospectra into the unstable right-half-plane. This penetration is induced by the non-orthogonality of multiple asymptotically stable eigenmodes and it indicates the potential of significant transient energy growth at small axial wave numbers.

We observe that wave-packet pseudomodes with larger axial wave numbers $\beta_*$ correspond to $\sigma$ far from the imaginary axis. If $\beta_*$ increases to infinity, the approximated rectangular region where the twist condition is satisfied will extend leftwards to be a semi-infinite rectangle. Any point in this rectangular region corresponds to a wave-packet pseudomode. It will be demonstrated shortly that the pseudomodes provide reasonable estimates eigenmodes of the matrix $\boldsymbol{D}$. The continuous nature of the region where pseudomodes exist further supports the existence of a continuous spectrum.

Figure 6 illustrates the distribution of point at fixed $\beta_*$ and $r_*$ where the twist condition is satisfied. Clearly, as $\beta_*$ increases, the points extend leftwards in the complex plane, while as $r_*$ increases, the points approach the imaginary line. This is consistent with the results discussed in section 5 that the radial frequencies of the eigenvectors increase as the point moves leftwards and the peak of energy of the eigenvectors moves radially outwards as the point approaches the real axis. We also note that there is a significant discrepancy
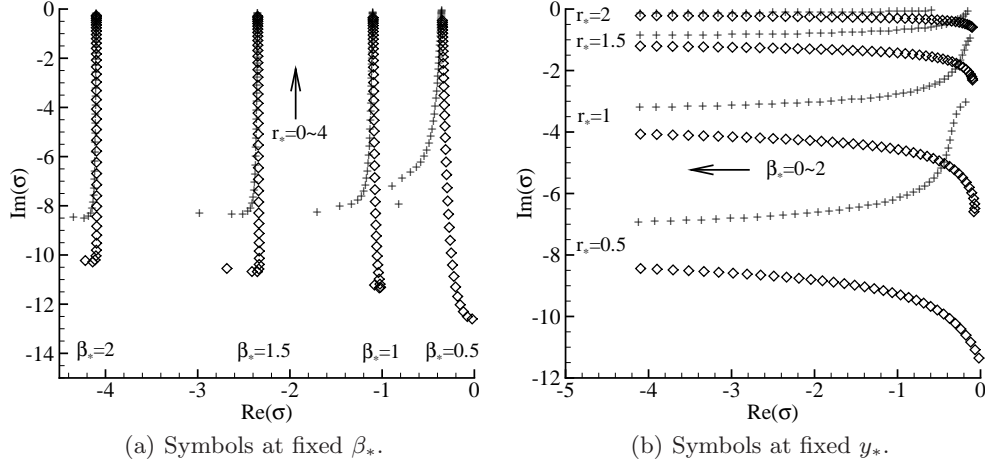
(a) Symbols at fixed $\beta_*$.  (b) Symbols at fixed $y_*$.

FIGURE 6. Symbols where the twist condition is satisfied at fixed $\beta_*$ and $r_*$. The symbols from solution (i) are denoted by "$\diamond$" while symbols from solution (ii) are denoted by "+". The arrows indicate the direction in which $\beta_*$ or $r_*$ increases.

between symbols from the two solutions, especially at the bottom of the rectangular region. This discrepancy indicates that some values of the symbol correspond to two pairs of $(\beta_*, r_*)$ and so the corresponding pseudomodes can be of the form of two wave packets. Since the discrepancy of wave numbers from the two solutions at a fixed symbol is not as apparent as the discrepancy of peak locations, the pseudomode with the form of two wave packets typically has two peaks and one wave number.

### 6.3. *Continuous modes approximated by wave-packet pseudomodes*

Although we have verified by the twist condition method that pseudomodes with wave packet forms exist in a continuous region, additional questions arise: are the predicted radial wave numbers and peak locations of the wave-packet pseudomodes accurate and are the pseudomodes sufficiently reasonable approximations of eigenmodes?

Figures 7a shows the radial frequency of the oscillating real/imaginary parts of an eigenmode of matrix $\boldsymbol{D}$ obtained from Fourier decomposition in the radial direction, while the radial distribution of this mode is shown in figure 7b (only the absolute value is presented for clarity). The eigenmode/eigenvalue chosen here is in the region where the discrepancy between the two solutions are small, so the eigenmode is of the form of one wave packet. The eigenmode/eigenvalue considered in figure 8 is in the region where the peak locations of the two predicted pseudomodes from the two solutions are separated, so the eigenmode are of the form of two wave packets. Clearly the wave-packet pseudomode method predicts the peak location and radial wave numbers of the eigenmodes reasonably well.

## 7. Conclusion

From the spectra of the evolution operator of the Batchelor vortex, three families of eigemodes can be identified: discrete modes, potential modes and free-stream modes. The convergence study supports the well documented observation that there is a discrete spectrum within the spectrum of the vortex flow. The energy of the discrete modes are commonly concentrated inside the vortex core, where the strain rate is maximised. All the asymptotically unstable modes of the Batchelor vortex are discrete modes, including
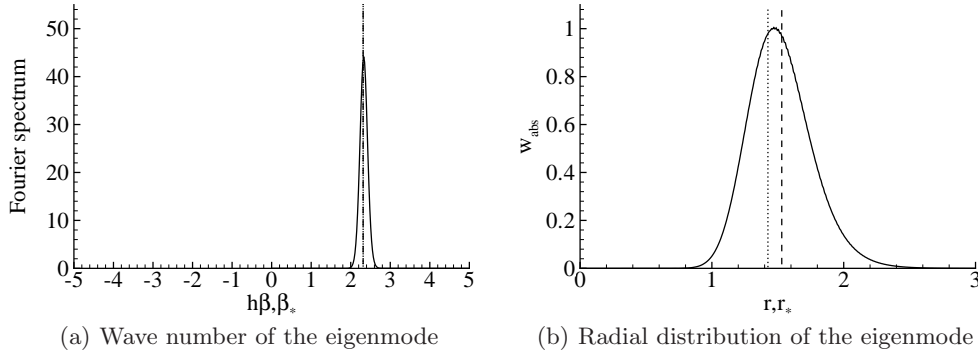
(a) Wave number of the eigenmode  (b) Radial distribution of the eigenmode

FIGURE 7. Eigenmode at $\sigma = -5.46 - 1.07i$ in the form of one wave packet. $\mathrm{w}_{abs} = |w|/\max_r|w|$. Predicted wave numbers and locations of the wave packets from two solutions are $(\beta_{*1}, r_{*1}) = (2.31, 1.53)$, denoted by the dashed line, and $(\beta_{*2}, r_{*2}) = (2.31, 1.43)$, denoted by the dotted line.
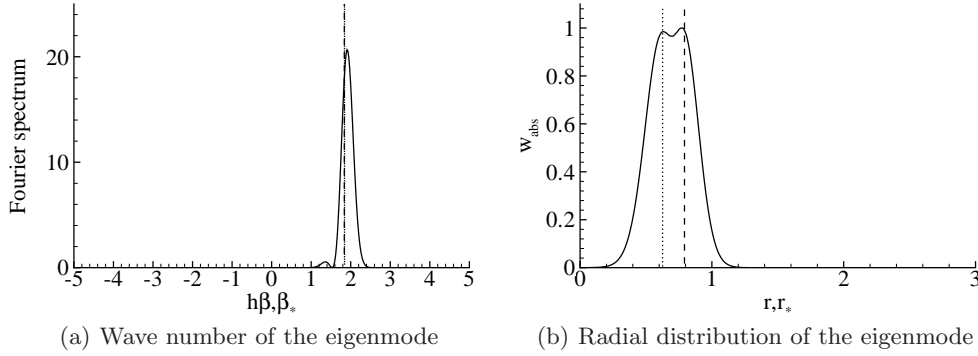


(a) Wave number of the eigenmode  (b) Radial distribution of the eigenmode

FIGURE 8. Eigenmode at $\sigma = -3.50 - 5.91i$ in the form of two wave packets. $\mathrm{w}_{abs} = |w|/\max_r|w|$. Predicted wave numbers and locations of the wave packets from two solutions are $(\beta_{*1}, r_{*1}) = (1.84, 0.792)$, denoted by the dashed line, and $(\beta_{*2}, r_{*2}) = (1.84, 0.626)$, denoted by the dotted line.

helical unstable modes (Lessen, Singh & Paillet 1974) and viscous centre unstable modes (Fabre & Jacquin 2004).

The potential modes correspond to a continuous spectrum and are asymptotically stable. However a combination of potential modes could generate strong transient growth (Obrist & Schmid 2003$b$; Mao 2010). This type of potential mode has also been reported by Obrist & Schmid (2003$a$) and Obrist & Schmid (2010) in their investigation of the lead-edge boundary layer flow.

When the radial decay rate of the potential modes tends to zero and the corresponding eigenvalues reach the real axis, the potential modes become free-stream modes. The free-stream mode oscillates in the free stream without radial decay. The existence of the free-stream modes is analytically verified and the corresponding spectrum is continuous ranging from $-\infty$ to $-k^2/Re$. In the inviscid limit or when the axial wave number tends to zero, the leading free-stream mode becomes neutrally stable. As the increase of the radial wave number and decrease of the axial wave number, free-stream modes penetrate into the vortex core and have the potential to transfer perturbations from free-stream turbulence into the vortex core (Zaki & Saha 2009).

The continuity of the potential mode spectrum is further confirmed by the wave-

packet pseudomode method, which indicates that pseudomodes with the form of wave packets exist in a semi-infinite rectangular region. The two branch nature of the governing pseudomode equation highlights that pseudomodes are of the form of either one or two wave packets. This method was also seen to predict the radial wave numbers and peak locations of the eigenmodes reasonably well.

## Appendix A. Linearised evolution operator

$$L_{vv} = Re(\frac{d^2}{dr^2} + \frac{d}{dr}/r - 1/r^2 - k^2),$$

$$L_{vw} = imRe(\frac{d}{dr}/r - 1/r^2),$$

$$L_{wv} = -im/k^2(\frac{d}{dr}/r + 1/r^2),$$

$$L_{ww} = 1 + \frac{m^2}{k^2r^2},$$

$$R_{vv} = \frac{d^4}{dr^4} + 2\frac{d^3}{dr^3}/r - (3/r^2 + f + k^2)\frac{d^2}{dr^2} + (3/r^3 - f/r - \frac{df}{dr} - k^2/r + ik\frac{dU}{dr}Re)\frac{d}{dr}$$
$$- 3/r^4 + f/r^2 - \frac{df}{dr}/r + k^2f + k^2/r^2 + ik\frac{d^2U}{dr^2}Re,$$

$$R_{vw} = i[m\frac{d^3}{dr^3}/r - 2m\frac{d^2}{dr^2}/r^2 + m(3/r^3 - f/r)\frac{d}{dr} - 3m/r^4$$
$$+ fm/r^2 - m\frac{df}{dr}/r + 2k^2m/r^2 + 2iWk^2Re/r],$$

$$R_{wv} = -i/Re/k^2[m\frac{d^3}{dr^3}/r + 2m\frac{d^2}{dr^2}/r^2 + (-fm/r - m/r^3)\frac{d}{dr}$$
$$+ m/r^4 - fm/r^2 + imk\frac{dU}{dr}Re/r - 2k^2m/r^2 - ik^2ERe],$$

$$R_{ww} = [(1 + \frac{m^2}{k^2r^2})\frac{d^2}{dr^2} + (1/r - \frac{m^2}{k^2r^3})\frac{d}{dr} - /r^2 - f - \frac{fm^2}{k^2r^2} + \frac{m^2}{k^2r^4}]/Re,$$

where $f = k^2 + m^2/r^2 + ikURe + imWRe/r$ and $E = W/r + \frac{dW}{dr}$.

## Appendix B. Existence and distribution of the free-stream spectrum

Here we will analytically present the existence and distribution of a free-stream spectrum in the vortex flow following the algorithm introduced by Gustavsson (1979). We start from the linearised Navier-Stokes equations (2.1) and consider the perturbation with axial wave number $k$ and azimuthal wave number $m$, denoted by $\tilde{\boldsymbol{u}}(k, r, m, t) = e^{i(kx+m\theta)}\boldsymbol{u}'(x, r, \theta, t)$. Applying a Fourier decomposition with respect to time $t$ gives

$$\boldsymbol{u}(k, r, m, \sigma) = (u, v, w) = \int_0^\infty e^{-\sigma t}\tilde{\boldsymbol{u}}(k, r, m, t)dt,$$

where $\sigma$ is the temporal growth rate of the perturbation and $u$, $v$ and $w$ represent the axial, radial and azimuthal components of $\boldsymbol{u}$. The transformed and linearised Navier-Stokes equations can be written as

$$\mathrm{i}ku + (\frac{d}{dr} + \frac{1}{r})v + \frac{\mathrm{i}m}{r}w = 0, \tag{B 1}$$

$$(\sigma + \mathrm{i}kU + \frac{\mathrm{i}mW}{r})u - u_0 + \frac{dU}{dr}v + \mathrm{i}kp = Re^{-1}(\frac{d^2}{dr^2} + \frac{1}{r}\frac{d}{dr} - k^2 - \frac{m^2}{r^2})u, \tag{B 2}$$

$$(\sigma + \mathrm{i}kU + \tfrac{\mathrm{i}mW}{r})v - v_0 - \tfrac{2W}{r}w + \tfrac{d}{dr}p$$
$$= Re^{-1}\left[(\tfrac{d^2}{dr^2} + \tfrac{1}{r}\tfrac{d}{dr} - k^2 - \tfrac{m^2+1}{r^2})v - \tfrac{2\mathrm{i}m}{r^2}w\right], \tag{B 3}$$

$$(\sigma + \mathrm{i}kU + \tfrac{\mathrm{i}mW}{r})w - w_0 + (\tfrac{W}{r} + \tfrac{dW}{dr})v + \tfrac{\mathrm{i}m}{r}p$$
$$= Re^{-1}\left[(\tfrac{d^2}{dr^2} + \tfrac{1}{r}\tfrac{d}{dr} - k^2 - \tfrac{m^2+1}{r^2})w + \tfrac{2\mathrm{i}m}{r^2}v\right], \tag{B 4}$$

where $(U, V, W)$ denote the base flow of the Batchelor vortex(see equation 1.1) and $(u_0, v_0, w_0)$ represent the initial perturbation: $(u_0, v_0, w_0) = (u, v, w)|_{t=0}$.

The free stream boundary conditions are $u = 0, v = 0$ and $w = 0$ and the boundary conditions imposed at $r = 0$ depend on the azimuthal wave number:

$$m = 0 : du/dr = v = w = dp/dr = 0, \tag{B 5}$$
$$m = -1 : u = v - \mathrm{i}w = dv/dr = p = 0, \tag{B 6}$$
$$m < -1 : u = v = w = p = 0. \tag{B 7}$$

In the far free stream, we assume $r \to \infty$ and so terms divided by $r$ tend to zero. Substituting equations (B 1) and (B 2) into equations (B 3) and (B 4) to eliminate the axial velocity component and pressure results in

$$\frac{d^4v}{dr^4} - (2k^2 + \sigma Re)\frac{d^2v}{dr^2} + (k^4 + \sigma k^2 Re)v = k^2 Re v_0, \tag{B 8}$$

$$\frac{d^2w}{dr^2} - (k^2 + \sigma Re)w = -w_0 Re. \tag{B 9}$$

We note that unlike the free-stream simplification of the O-S equations where both the streamwise and spanwise wave numbers appear explicitly, all the terms related to the azimuthal wave number $m$ vanish in the free-stream equations (B 8)-(B 9). Considering the boundary conditions given in equations (B 6)-(B 7), the boundary conditions at $r = 0$ for equations (B 8)-(B 9) can be obtained by differentiating equation (B 1) twice, while the conditions at $r \to \infty$ can be obtained from equation (B 1) directly

$$r = 0 : v = w = \frac{d^2v}{dr^2} = 0 \quad \text{and} \quad r = \infty : v = w = \frac{dv}{dr} = 0. \tag{B 10}$$

Equation (B 8) has four homogeneous solutions: $v_1 = e^{-kr}$, $v_2 = e^{-\lambda r}$, $v_3 = e^{kr}$ and $v_4 = e^{\lambda r}$ where

$$\lambda^2 = k^2 + \sigma Re. \tag{B 11}$$

Due to the symmetry of the problem, we only need to consider the case when $k > 0$ and $Re(\lambda) > 0$.

Using the method of variation parameters, solutions to equation (B 8) can be written as

$$v = A_1 v_1 + A_2 v_2 + A_3 v_3 + A_4 v_4. \tag{B 12}$$

$A_i$ satisfies

$$N \frac{dA}{dr} = B, \tag{B 13}$$

where

$$
N = \begin{bmatrix}
v_1 & v_2 & v_3 & v_4 \\[2mm]
\frac{dv_1}{dr} & \frac{dv_2}{dr} & \frac{dv_3}{dr} & \frac{dv_4}{dr} \\[2mm]
\frac{d^2 v_1}{dr^2} & \frac{d^2 v_2}{dr^2} & \frac{d^2 v_3}{dr^2} & \frac{d^2 v_4}{dr^2} \\[2mm]
\frac{d^3 v_1}{dr^3} & \frac{d^3 v_2}{dr^3} & \frac{d^3 v_3}{dr^3} & \frac{d^3 v_4}{dr^3}
\end{bmatrix}, \qquad
A = \begin{bmatrix} A_1 \\[2mm] A_2 \\[2mm] A_3 \\[2mm] A_4 \end{bmatrix}, \qquad
B = \begin{bmatrix} 0 \\[2mm] 0 \\[2mm] 0 \\[2mm] k^2 v_0 Re \end{bmatrix}.
$$

Solve equation (B 13) by application of the Crammer's rule, we obtain

$$A_i = \int_{r_i}^{r} D_i k^2 v_0 Re/\omega \, dy, \qquad i = 1, 2, 3, 4 \tag{B 14}$$

where $D_i$ is the cofactor of $d^3 v_i/dr^3$ and $\omega$ is the Wronskian. Here $D_1 = -2\lambda\sigma e^{kr} Re$, $D_2 = 2k\sigma e^{\lambda r} Re$, $D_3 = 2\lambda\sigma e^{-kr} Re$, $D_4 = -2k\sigma e^{-\lambda r} Re$ and $\omega = |N| = -4k\lambda\sigma^2 Re^2$.

Substituting equation (B 14) into equation (B 12) and applying the boundary conditions defined in equation (B 10) result in

$$v = \frac{-k}{4\lambda\sigma^2 Re} [v_1(a_1 + \int_0^r D_1 v_0 dy) + v_2(a_2 + \int_0^r D_2 v_0 dy) + v_3 \int_\infty^r D_3 v_0 dy + v_4 \int_\infty^r D_4 v_0 dy], \tag{B 15}$$

where

$$a_1 = \frac{a_3[v_{20}(\frac{d^2 v_3}{dr^2})_0 - (\frac{d^2 v_2}{dr^2})_0 v_{30}] + a_4[v_{20}(\frac{d^2 v_4}{dr^2})_0 - (\frac{d^2 v_2}{dr^2})_0 v_{40}]}{v_{10}(\frac{d^2 v_2}{dr^2})_0 - (\frac{d^2 v_1}{dr^2})_0 v_{20}},$$

$$a_2 = -\frac{a_3[v_{10}(\frac{d^2 v_3}{dr^2})_0 - (\frac{d^2 v_1}{dr^2})_0 v_{30}] + a_4[v_{10}(\frac{d^2 v_4}{dr^2})_0 - (\frac{d^2 v_1}{dr^2})_0 v_{40}]}{v_{10}(\frac{d^2 v_2}{dr^2})_0 - (\frac{d^2 v_1}{dr^2})_0 v_{20}},$$

$$a_3 = \int_\infty^0 D_3 v_0 dy = -a_1,$$

$$a_4 = \int_\infty^0 D_4 v_0 dy = -a_2.$$

The subscript 0 denotes the value at $r = 0$. Here $\sum_{i=1}^{4} D_i v_i = 0$ and $\sum_{i=1}^{4} D_i \frac{dv_i}{dr} = 0$ are used.

Similarly, solve equations (B 9, B 10), we obtain

$$w = \frac{Re}{2\lambda}\left[v_2\left(\int_\infty^0 w_0 e^{-\lambda y} dy + \int_0^r w_0 e^{\lambda y} dy\right) - v_4 \int_\infty^r w_0 e^{-\lambda y} dy\right]. \tag{B 16}$$
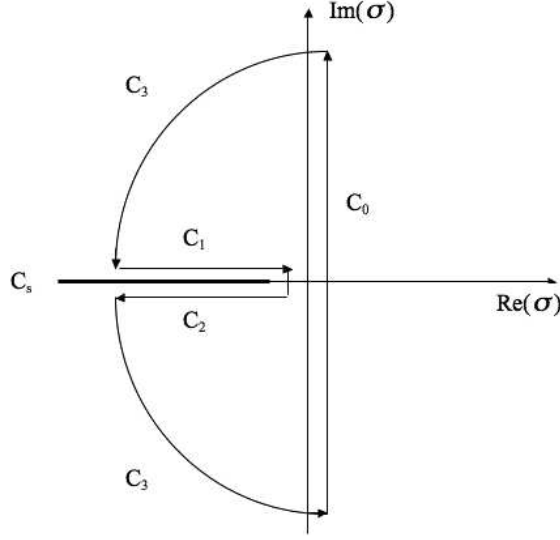
FIGURE 9. Integration contour of inverse Laplace transformation.

The axial velocity can then be obtained from equation (B 1) as

$$u = -\frac{\mathrm{i}}{k}\frac{dv}{dr}.$$

We need to invert the Laplace transformation to establish the time dependence of the modes explicitly:

$$\tilde{\boldsymbol{u}} = \frac{1}{2\pi\mathrm{i}}\int_{\gamma-\mathrm{i}\infty}^{\gamma+\mathrm{i}\infty} e^{\sigma t}\boldsymbol{u}d\sigma,$$

The path of integration must be to the right of all the singularities and this path is denoted by $C_0$ in figure 9.

There are three singularities in equation (B 15): $v_{10}(\frac{d^2 v_2}{dr^2})_0 - (\frac{d^2 v_1}{dr^2})_0 v_{20} = 0$, $\sigma = 0$ and $\lambda = 0$. The first two singularities are the same condition, since when $\sigma = 0$ the first condition is also satisfied. Further, under these conditions the homogeneous solutions should also be modified to one without singularities. Actually we see from equation (B 11) that when $\sigma = 0$, $\lambda = k$, and so $(v_1, v_2, v_3, v_4)$ becomes dependent, and therefore a different representation of homogeneous solutions must be used, for example $v_1 = e^{-kr}$, $v_2 = e^{kr}$, $v_3 = re^{kr}$ and $v_4 = re^{-kr}$. In this case, the Wronskian $\omega = 16k^4$, does not have any singularity.

Therefore, the only relevant singularity of equation (B 15) in the real analysis is $\lambda = 0$. Then we establish that in the complex analysis, $\lambda = 0$ represents the end of a branch cut singularity. Considering $\lambda = \lambda_r + \mathrm{i}\lambda_i$ and $\lambda_r > 0$ due to the symmetry as we discussed before, from equation (B 11) we have

$$\sigma = (\lambda_r^2 - \lambda_i^2 - k^2)/Re + \frac{2\lambda_r\lambda_i}{Re}\mathrm{i}.$$

Then $\lambda$ is a multivalued function of $\sigma$ when $\lambda_r \to 0$ because in equation (B) each value of $\sigma$ corresponds to two values of $\lambda_i$. This one-to-many mapping results in a discontinuity of $\lambda$ across the branch cut represented by the line ($C_s$ in figure 9) where

$$\sigma = -(n^2 + k^2)/Re, \qquad 0 < n = |\lambda_i| < \infty.$$

When this branch cut is approached from above, we observe that $\lambda \to \mathrm{i}n$, while if this line is approached from below, $\lambda \to -\mathrm{i}n$. Hence, we have a branch line lying on the left of $\sigma = -k^2/Re$ associated with the singularity of $\lambda = 0$, so the integration contour must be deformed to go around the branch cut, as shown in figure 9. The modes corresponding to the values on $C_s$ have the form $v \sim e^{\lambda r}$, so $n$ can be interpreted as the radial wave number of the modes.

Applying the inverse Laplace transformation, it follows that

$$2\pi i \tilde{\boldsymbol{u}} = \int_{C_0} e^{\sigma t} \boldsymbol{u} d\sigma = -\int_{C_1} e^{\sigma t} \boldsymbol{u} d\sigma - \int_{C_2} e^{\sigma t} \boldsymbol{u} d\sigma,$$

where $\lambda = \mathrm{i}n$ in the integration along $C_1$ and $\lambda = -\mathrm{i}n$ along $C_2$.

The thick line denoted as $C_s$ in figure 9 represents the free-stream spectrum of equations (B 8)-(B 10). Because this branch cut is the only singularity of equations (B 8)-(B 10), modes associated with values along the line $C_s$ are the only modes in the far free stream of the vortex flow under the initial assumption of this analysis.

With the increase of the Reynolds number and decrease of the axial wave number, the free-stream spectrum, whose right end point is $-k^2/Re$, approaches the imaginary axis. When $k \to 0$ or $Re \to \infty$, the leading free-stream modes become neutrally stable.

## Appendix C. Variables in equation (6.1)

After substituting the base flow velocity expressions of the Batchelor vortex, the variables in the symbol equation (6.1) can be written as

$$
\begin{aligned}
\mathcal{F} =& (-\frac{\beta^2}{h^2} + \frac{\mathrm{i}\beta}{rh} - \frac{1}{r^2} - k^2)/\nu, \\
\mathcal{M} =& \frac{\beta^4}{h^4} - \frac{2\mathrm{i}\beta^3}{rh^3} + \frac{\beta^2}{h^2}(\frac{3}{r^2} + 2k^2) + \frac{\mathrm{i}\beta}{h}(\frac{3}{r^3} - \frac{2k^2}{r}) - \frac{3}{r^4} + \frac{2k^2}{r^2} + k^4 \\
& - \frac{\mathrm{i}k}{\nu}[U(-\frac{\beta^2}{h^2} + \frac{\mathrm{i}\beta}{rh} - \frac{1}{r^2} - k^2) + \frac{1}{r}\frac{dU}{dr} - \frac{d^2U}{dr^2}] \\
=& \frac{\beta^4}{h^4} - \frac{2\mathrm{i}\beta^3}{rh^3} + \frac{\beta^2}{h^2}(\frac{3}{r^2} + 2k^2) + \frac{\mathrm{i}\beta}{h}(\frac{3}{r^3} - \frac{2k^2}{r}) - \frac{3}{r^4} + \frac{2k^2}{r^2} + k^4 \\
& - \frac{\mathrm{i}k}{\nu}e^{-r^2}(-\frac{\beta^2}{h^2} + \frac{\mathrm{i}\beta}{rh} - \frac{1}{r^2} - k^2 - 4r^2), \\
\mathcal{G} =& - 2k^2/\nu/r = -\frac{2qk^2(1 - e^{-r^2})}{r^2\nu}, \\
\mathcal{E} =& - \Phi = -2qe^{-r^2}, \\
\mathcal{H} =& (-\frac{\beta^2}{h^2} + \frac{\mathrm{i}\beta}{rh} - \frac{1}{r^2} - k^2)\nu - \mathrm{i}kU = (-\frac{\beta^2}{h^2} + \frac{\mathrm{i}\beta}{rh} - \frac{1}{r^2} - k^2)\nu - \mathrm{i}ke^{-r^2}.
\end{aligned}
$$

REFERENCES

ABID, M. 2008 Nonlinear mode selection in a model of trailing line vortices. *J. Fluid Mech.* **605**, 1945.

BATCHELOR, G. K. 1964 Axial flow in trailing line vortices. *J. Fluid Mech.* **20**, 645–658.

BENDER, C.M. & ORSZAG, S.A. 1978 *Advanced Mathematical Methods for Scientists and Engineers*. McGrawHill.

BOYD, J.P. 2001 *Chebyshev and Fourier Spectrum Methods*. Dover, New York.

FABRE, D. & JACQUIN, L. 2004 Viscous instabilities in trailing vortices at large swirl numbers. *J. Fluid Mech.* **500**, 239–262.

FABRE, D., SIPP, D. & JACQUIN, L. 2006 Kelvin waves and the singular modes of the Lamb-Oseen vortex. *J. Fluid Mech.* **551**, 235–274.

GROSCH, C. E. & SALWEN, H. 1978 The continuous spectrum of the Orr–Sommerfeld equation. Part 1. The spectrum and the eigenfunctions. *J. Fluid Mech.* **87**, 33–54.

GUSTAVSSON, L. H. 1979 Initial–value problem for boundary layer flows. *Phys. Fluids* **22**, 1602–1605.

HEATON, C. J. 2007 Centre modes in inviscid swirling flows and their application to the stability of the Batchelor vortex. *J. Fluid Mech.* **576**, 325–348.

HEINRICHS, W. 1989 Improved condition number for spectral methods. *Mathematics of computation* **53**, 103–119.

HEINRICHS, W. 1991 A stabilized treatment of the biharmonic operator with spectral methods. *SIAM Journal on Scientific and Statistical Computing* **12**, 1162–1172.

JORDINSON, R. 1970 Spectrum of eigenvalues of the Orr–Sommerfeld equation for Blasius flow. *Phys. Fluids* **14**, 2535–2537.

JOSHI, S. S. 1996 A systems theory approach to the control of plane Poiseuille flow. PhD thesis, Department of Electrical Engineering, UCLA.

KHORRAMI, M. R. 1991 On the viscous modes of instability of a trailing line vortex. *J. Fluid Mech.* **225**, 197–212.

KHORRAMI, M. R. 1992 Behavior of asymmetric unstable modes of a trailing line vortex near the upper neutral curve. *Phys. Fluids A* **4**, 13101313.

LE DIZÉS, S. & FABRE, D. 2010 Viscous ring modes in vortices with axial jet. *Theoret. Comput. Fluid Dynamics* **24**, 349361.

LESSEN, M. & PAILLET, F. 1974 The stability of a trailing line vortex. Part 2. Viscous theory. *J. Fluid Mech.* **65**, 769–779.

LESSEN, M., SINGH, P. J. & PAILLET, F. 1974 The stability of a trailing line vortex. Part 1. Inviscid theory. *J. Fluid Mech.* **63**, 753–763.

MACK, L. M. 1976 A numerical study of the temporal eigenvalue spectrum of the Blasius boundary layer. *J. Fluid Mech.* **73**, 497–520.

MAO, XUERUI 2010 Vortex instability and transient growth. PhD thesis, Imperial College London.

MCKERNAN, J. 2006 Control of plane Poiseuille flow: a theoretical and computational investigation. PhD thesis, Department of Aerospace Sciences, School of Engineering, Cranfield University.

OBRIST, D. & SCHMID, P. 2008 Resonance in the cochleawithwave packet pseudomodes. In *XXII ICTAM*.

OBRIST, D. & SCHMID, P. 2009 Wave packet pseudomodes upstream of a swept cylinder. In *Seventh IUTAM Symposium on Laminar-Turbulent Transition*.

OBRIST, D. & SCHMID, P. J. 2003*a* On the linear stability of swept attachment-line boundary layer flow. Part 1. Spectrum and asymptotic behaviour. *J. Fluid Mech.* **493**, 1–29.

OBRIST, D. & SCHMID, P. J. 2003*b* On the linear stability of swept attachment-line boundary layer flow. Part 2. Non–modal effects and receptivity. *J. Fluid Mech.* **493**, 31–58.

OBRIST, D. & SCHMID, P. J. 2010 Algebraically decaying modes and wave packet pseudo-modes in swept Hiemenz flow. *J. Fluid Mech.* **643**, 309–332.

RAYLEIGH, L. 1916 On the dynamics of revolving fluids. *Proc. R. Soc. Lond. A* **93**, 148–154.

SCHMID, PETER JOHANNES & HENNINGSON, DAN S. 2001 *Stability and Transition in Shear Flows*. Springer.

TREFETHEN, L. N. 2005 Wave packet pseudomodes of variable coefficient differential operators. *Proc. R. Soc. A* **461**, 30993122.

WEIDEMAN, J. A. C. & REDDY, S. C. 2000 A MATLAB differentiation matrix suite. *ACM Transactions on Mathematical Software* **26**, 465–519.

ZAKI, T. A. & SAHA, S. 2009 On shear sheltering and the structure of vortical modes in single– and two–fluid boundary layers. *J. Fluid Mech.* **626**, 111–147.